Catalysis Science & Technology

Accepted Manuscript

ROYAL SOCIETY OF CHEMISTRY

www.rsc.org/catalysis

Journal Name

RSCPublishing

ARTICLE

Redox-stable chromate cathode decorated with *in situ* grown nickel nanocatalyst towards efficient carbon dioxide electrolysis

Cite this: DOI: 10.1039/xoxxooooox

Received ooth January 2012,
Accepted ooth January 2012

DOI: 10.1039/xoxxooooox

www.rsc.org/

Cong Ruan [a] and Kui Xie [a, b] *

Redox-stable $La_{0.75}Sr_{0.25}Cr_{0.5}Mn_{0.5}O_{3-\delta}$ (LSCM) ceramic can be utilized as a solid oxide electrolyzer cathode for direct carbon dioxide electrolysis; nevertheless, the insufficient electro-catalytic activity of ceramic LSCM restricts the electrode performances and current efficiencies. In this paper, catalytic-active nickel nanoparticles are anchored on the surface of LSCM substrate through *in situ* growing process to improve electrode performances. The combined analyses of XRD, TEM, XPS, SEM and EDS demonstrate the reversible *in situ* growth of nickel catalyst by transforming A-site deficient and B-site excess $(La_{0.75}Sr_{0.25})_{0.9}(Cr_{0.5}Mn_{0.5})_{0.9}Ni_{0.1}O_{3-\delta}$ (LSCMN) to LSCM and nickel in redox cycles. The conductivities of LSCM and LSCMN are investigated and correlated with electrode performances in symmetrical cells and electrolysis cells. Significant improvement in electrode polarization resistance has been observed for the LSCMN cathode. The current efficiency is considerably improved by 30% with LSCMN in contrast to bare LSCM cathode for direct carbon dioxide electrolysis at 800 ºC.

Introduction

Recently, solid oxide electrolyzer has been paid a lot of attention because of its enormous advantages of efficient electrochemical conversion of CO_2 into fuels using renewable electrical energy, which provides an alternative for producing renewable fuels.[1–5] High temperature CO_2 electrolysis in an oxide-ion-conducting solid oxide electrolyzer is of great advantage because it can directly electrolyze CO_2 into CO and oxygen under external voltages. In this process, the CO_2 is electrochemically reduced into CO and oxide ion at cathode and the O^{2-} transports through electrolyte to anode to form oxygen gas.[6,7] High operation temperatures ranging from 700 to 1000 ºC are of great promise in the CO_2 electrolysis process for the reason that heat partly offers the energy for molecular dissociation which leads to favorable kinetics and thermodynamics even without using expensive noble metals as electrodes.[8,9]

Traditional Ni-YSZ composite cathode has been widely used in the oxide-ion-conducting solid oxide electrolyzers because of its excellent performances for high temperature CO_2

electrolysis.[3,10,11] Irvine *et al.* had investigated the Ni-YSZ composite cathode for CO_2 electrolysis in solid oxide electrolyzers, and found that the current density of 0.8 $A \cdot cm^{-2}$ had been achieved in CO_2/CO atmospheres under 2.25 V at 900 ºC.[6] Barnett *et al.* had also performed coelectrolysis of CO_2/H_2O using the solid oxide electrolyzers based on Ni-YSZ cathode and yielded a syngas production rate of about 7 $sccm \cdot cm^{-2}$ in 25% H_2, 25% CO_2 and 50% H_2O under 1.3 V at 800 ºC.[12] It is obvious that a significant concentration of reducing gas is demanded to flow over the Ni-YSZ cathodes to avoid the oxidation of nickel. The inherent redox instability of Ni-YSZ would lead to the loss of electronic conductivity and even the failure of the electrode, which has become the limitation of electrode performances.[13,14] Recently, it has been reported that the perovskite-type ceramic $La_{0.75}Sr_{0.25}Cr_{0.5}Mn_{0.5}O_{3-\delta}$ (LSCM) is a promising cathode material for its excellent redox stability and catalytic activity compared to the traditional Ni-YSZ.[15–18] Direct CO_2 electrolysis with electrolyzers based on LSCM cathode has been investigated in previous works, promising electrode performances and current efficiencies without the flow of reducing gas over the cathode have been demonstrated.[9,19] Yue *et al.* had demonstrated the excellent performances of CO_2 electrolysis in high temperature solid oxide electrolyzers based on LSCM composite cathode, the CO production rate of approximately 1.2 $\mu mol \cdot s^{-1}$ and the Faraday efficiency of 96% had been obtained in CO_2/CO atmospheres under 1.0 V at 900 ºC.[20] However, the cathode performances are restricted by the insufficient electro-catalytic activity of LSCM. For this reason, it is of great importance to enhance the electro-catalytic activity of the LSCM electrode in order to improve the performances of direct CO_2 electrolysis.[21]

Traditional Ni, Fe, Cu and *etc.* have been commonly utilized as excellent catalysts in many fields such as biogas reforming, water gas shift reaction and catalytic conversion of CO_2.[22,23] Among these elements, nickel is a well-known catalyst for its excellent catalytic activity in heterogeneous catalysis, electrochemistry and fuel cells.[24,25] Caldes *et al.* had achieved the improved electrochemical characteristics of the electrodes doped with a small amount of nickel nanocatalyst. They found that the total conductivities of the nickel doped LSCM-based materials had been improved to 36 $S \cdot cm^{-1}$ for $LSCM_{0.44}N_{0.06}$ and 24 $S \cdot cm^{-1}$ for $LSC_{0.44}MN_{0.06}$ compared to 13 $S \cdot cm^{-1}$ of bare LSCM.[25] These metal nanocatalysts can be added into the electrode by impregnation with a metallic salt or a nanopowder suspension, or precipitating with metal nano-clusters on the electrode surface; besides, *in situ* growth of metal nanoparticles is also an alternative route to coat the nanocatalyst onto the substrate.[26] Irvine *et al.* had recently reported that uniformly dispersed nanoparticles could be decorated on the surface by *in situ* growing the nanoparticles directly from the (porous) backbone support. They had demonstrated that the growing nano-size phases from perovskites can be controlled by tuning deviations from the ideal ABO_3 stoichiometry, such as A-site-deficient perovskites (A/B < 1). A-site deficiency would offer driving force for the B-site exsolution for the reason that in this system B-site exsolution tends to locally revert the perovskite towards a stable, 'defect-free' ABO_3 stoichiometry.[26]

In this work, nickel is introduced into the B-site of LSCM lattice to form the A-site deficiency and B-site excess $(La_{0.75}Sr_{0.25})_{0.9}(Cr_{0.5}Mn_{0.5})_{0.9}Ni_{0.1}O_{3-\delta}$ (LSCMN). The crystal structures and reversible exsolution of nickel nanoparticles are investigated and correlated to the electrical properties of the

samples. Direct CO_2 electrolysis is then investigated with LSCM and LSCMN cathodes at 800 ºC, respectively.

Experimental

All the chemicals (99.9%) were bought from Sinopharm Chemical Reagent Co., Ltd (China) unless otherwise specified. The LSCM powders were synthesized through a combustion method with stoichiometric amounts of La_2O_3, $SrCO_3$, $Cr(NO_3)_3 \cdot 9H_2O$, $C_4H_6MnO_4 \cdot 4H_2O$ and glycine followed by a heat treatment at 1200 ºC (2 ºC·min^{-1}) for 5 h in air as described elsewhere, and the LSCMN powders were synthesized through the same method as LSCM with extra NiO.[27,28] The $(La_{0.8}Sr_{0.2})_{0.95}MnO_{3-\delta}$ (LSMO) powders were prepared through the same method as described above with stoichiometric amounts of La_2O_3, $SrCO_3$, $C_4H_6MnO_4 \cdot 4H_2O$ and glycine followed by a heat treatment at 1100 ºC (2 ºC·min^{-1}) for 3 h in air.[29] The combustion method was also employed for the synthesis of $Ce_{0.8}Sm_{0.2}O_{2-\delta}$ (SDC) powders with stoichiometric amounts of Sm_2O_3, $Ce(NO_3)_3 \cdot 6H_2O$ and glycine followed by a heat treatment at 800 ºC (2 ºC·min^{-1}) for 3 h in air.[30] X-ray diffraction (XRD, Cu K_α, 2θ = 3º·min^{-1}, D/MAX2500V, Rigaku Corporation, Japan) was employed for analyzing the phase formations of LSCM, LSCMN, LSM and SDC powders with 2θ ranging from 10° to 90°, and the XRD Rietveld refinement was performed using General Structure Analysis System (GSAS) software.[31] High-resolution transmission electron microscopy (HRTEM, JEM-2100F, JEOL Ltd, Japan) analysis with selected area diffraction was performed to investigate the microstructures of oxidized and reduced LSCM and LSCMN powders. X-ray photoelectron spectroscopy (XPS, ESCALAB25, Thermo, USA) was handled using monochromatized Al Kα at *hv* = 1486.6 eV to analyze the chemical states of oxidized and reduced LSCM and LSCMN powders with the binding energies calibrated to the C 1s peak at 285 eV.

About 2.0 g LSCM or LSCMN powders were pressed into a bar followed with a heat treatment at 1400 ºC (2 ºC·min^{-1}) for 10 h in air for the conductivity tests. The conductivity test was operated through the DC four-terminal method with a LSCM or LSCMN bar mounted by four Ag wires (0.4 mm in diameter) using the conductive adhesive (DAD87, Shanghai Research Institute for Synthetic Resins, Shanghai, China) followed with a heat treatment at 550 °C (3 ºC·min^{-1}) for 30 min in air, and the bar was connected to a four terminal jig coupled with an oxygen sensor device. The conductivities of LSCM and LSCMN *versus* temperature in air were measured from approximately 200 to 800 °C (3 ºC·min^{-1}) using an online multi-meter (Keithley 2000, Digital Multimeter, Keithley Instrument Inc., USA). The dependence of conductivity on the oxygen partial pressure (pO_2) was tested at 800 °C with pO_2 reducing from 10^{-1} to 10^{-18} atm by flowing 5%H_2/Ar over the sample regulated using a mass flow meter (D08-3F, Sevenstar, China) at the rate of 25 ml·min^{-1}, and pO_2 was recorded by an online sensor (Type 1231, ZrO_2-based oxygen sensor, Noveltech, Australia). The conductivities of LSCM and LSCMN *versus* temperature were also tested in the reducing atmosphere with the temperature ranging from 300 to 800 ºC.

The YSZ powders were dry-pressed into green disks with the diameter of ~ 20 mm and the thickness of ~ 1 mm followed by a heat treatment at 1500 ºC (2 ºC·min^{-1}) for 10 h in air.[32] The sintered YSZ disks were then mechanically polished using sand paper (1000 mesh) and ultrasonically cleaned for several times in the ethanol and distilled water followed by drying in air overnight to get the YSZ electrolyte supports. The composite cathode slurry of LSCM/SDC or LSCMN/SDC was prepared

by milling the LSCM or LSCMN powders with the SDC powders at a ratio of 65/35 wt% directly in alpha-terpineol in a mortar, and the cellulose was added to make electrode porous in the meantime. The anode slurry was made in the same way with the LSM powders. After that, the LSCM or LSCMN slurry was printed onto one side of the prepared YSZ electrolyte support with an area of about 1 cm^2, then the symmetrical cell was prepared by printing the same slurry onto the other side and the single cell was prepared by printing the LSM slurry onto the other side served as the anode followed by a heat treatment at 1000 ºC (2 ºC·min^{-1}) for 3 h in air. The current collection layers were made by printing silver paste (SS-8060, Xinluyi, Shanghai, China) on both surfaces of the electrode, and the external circuit was made with silver wires fastened to both current collectors using conductive adhesive followed by heating at 550 ºC (3 ºC·min^{-1}) for 30 min in air. The microstructure of the as-prepared electrolyzer was observed with scanning electron microscope (SEM, JSM-6490LV, JEOL Ltd, Japan).

The mixed conductivities of the porous LSCM and LSCMN electrodes supported on YSZ disks were tested in the redox-cycling atmospheres with air as the oxidizing atmosphere and 5%H_2/Ar as the reducing atmosphere at 800 ºC. The sample for the test was obtained by printing the as-prepared cathode slurry onto the entire surface of the YSZ electrolyte support followed by a heat treatment at 1000 ºC (2 ºC·min^{-1}) for 3 h in air, then draw four equidistant lines on the surface of the electrode with silver paste, and each silver line was fastened by a silver wire with the conductive adhesive followed by a heat treatment at 550 ºC (3 ºC·min^{-1}) for 30 min in air. The AC impedance of the symmetrical cells *versus* hydrogen partial pressure (pH_2) were tested (2-electrode mode) using an electrochemical station (IM6, Zahner, Germany) under the open circuit voltage (OCV) in different pH_2 at 800 ºC (frequency of 1 M–0.1 Hz, signal strength of 10 mA), and the pH_2 was adjust by changing the ratio of H_2 and N_2 with the aid of the mass flow meters (flow rate of 20 ml·min^{-1}). The AC impedance spectra of the symmetrical cells *versus* CO partial pressure (pCO) were carried out in the same way. The electrolyzer was sealed to a home-made testing jig using ceramic paste (JD-767, Jiudian, Dongguan, China) for electrochemical measurements. The CO_2 electrolysis with the electrolyzers based on LSCM and LSCMN cathodes were preformed (2-electrode type) in pure CO_2 (15 ml·min^{-1}) at 800 ºC. The current-voltage curves (I-V, 0.007 V·s^{-1}) and the AC impedance spectroscopies (1 M–0.1 Hz, 10 mV) were recorded using the electrochemical station, and the productions of CO were analyzed using an online gas chromatograph (GC9790II, Fuli, Zhejiang, China) with the output gas from the cathodes.

Results and discussion

Figs. 1 (a1) and (a2) show the XRD Rietveld refinement patterns of the oxidized and reduced LSCM powders, respectively. The chi^2, wRp and Rp values of 2.096, 11.59% and 8.68% as well as 2.146, 11.65% and 8.54% are given by the refinement for the oxidized LSCM and for the reduced LSCM sample, respectively, which are well consistent with the reported data in the previous work.[33] The refinement data and the experimental results indicate that the phase structure of the oxidized as well as reduced samples can both be determined as perovskite structure with space group of R-3c and SG number of 167.[33] As shown in Figs. 1 (a1) and (a2), according to the refinement, the crystal cell parameters are a = b = 5.491 Å, c = 13.319 Å and V = 347.796 $Å^3$ for the oxidized LSCM and a = b = 5.496 Å, c = 13.321 Å and V = 348.208 $Å^3$ for the reduced

LSCM, respectively. The slight increase of the crystal cell parameters after high-temperature reduction is probably due to the transformation of Cr^{6+} (0.44 Å) and Mn^{4+} (0.53 Å) to Cr^{3+} (0.615 Å) and Mn^{3+} (0.645 Å), which may cause the lattice expansion though the oxygen loss is present.[31] However, no phase transition is observed in LSCM after the high-temperature treatment in a very reducing atmosphere, which firmly indicates the superior redox stability of LSCM. The XRD refinement patterns of the oxidized and reduced LSCMN powders are displayed in Figs. 1 (b1) and (b2), respectively. No extra peak is observed for the oxidized LSCMN, which indicates the successful partial replacement by nickel in the B-site of cell lattice. The crystal cell parameters of the oxidized LSCMN are slightly larger than those of the oxidized LSCM, which is because of the larger ionic radii of the Ni^{2+} (0.69 Å) compared with the Cr^{6+} (0.44 Å) and Mn^{4+} (0.53 Å) with the same coordination numbers. As shown in Fig. 1 (b2), the peak at $2\theta = 44.5^{o}$ corresponded to the nickel (PDF: 45-1027) indicates the successful exsolution of nickel metal from LSCM substrate, which also suggests excellent stability of the parent material LSCM even though the doped metal is exsolved. What's more, the crystal cell parameters of LSCMN display a similar trend as LSCM after high-temperature reduction and that is also because of the partial transformation of the Cr^{6+} and Mn^{4+} into $Cr^{3+/4+}$ and Mn^{3+} leading to the lattice expansion of the reduced LSCMN even the nickel is exsolved out of the lattice.

Figs. 2 (a1) and (a2) show the HRTEM analyses of the oxidized and reduced LSCM, which have displayed the lattice spacing of 0.2777 nm (110) for oxidized LSCM and 0.2781 nm (110) for reduced LSCM, and the separation spacing is consistent well with the crystal cell parameters determined by the XRD analyses shown in Figs. 1 (a1) and (a2). The HRTEM analyses of the oxidized and reduced LSCMN are shown in Figs. 2 (b1) and (b2). The corresponding lattice spacing of the LSCMN substrate increases from 0.2799 to 0.2815 nm (110) after reduction, and that further demonstrates the lattice expansion of the reduced sample as determined by the XRD analyses shown in Figs. 1 (b1) and (b2), and the increase of the corresponding lattice spacing (110) of LSCM from 0.2777 to 0.2799 nm with nickel doped into the substrate firmly confirms the lattice expansion caused by nickel doping as determined above by the XRD analysis. What's more, the *in situ* growth of nickel nanoparticles anchored on the LSCM surface after high-temperature reduction can be clearly observed in Fig. 2 (b2), and the analysis result reveals that the corresponding lattice spacing of nickel is 0.2053 nm (011), which is consistent well with the standard XRD data (PDF: 45-1027). In the *in situ* growth of nanoparticles as reported by Irvine *et al.*, at an atomic scale, by reducing an A-site deficiency and B-site excess perovskite, oxygen vacancies are introduced, which may seclude the B-site dopants (namely nickel nanocatalyst in our work) from the main perovskite framework into an incipient exsolution. In the reduced LSCMN unit cell, the occupied A-sites are left unaltered and the initial apparent B-site excess is expelled, which shows how anchoring between the nucleating nickel nanoparticles and parent LSCM substrate.[26] Figs. 2 (b3) and (b4) illustrate more minutely that the nickel nanoparticles are anchored on the LSCM substrate.

In order to investigate the elemental valence state change, XPS spectra of the oxidized and reduced LSCM and LSCMN are obtained as the core level spectroscopies for the Ni 2p, Cr 2p and Mn 2p as shown in the Figs. 3 and 4. All of these XPS spectra are fitted through a Shirley-type background subtraction

method with the background functions for different spectra of the elements fitted by 80% Gaussian and 20% Lorenzial. The core level XPS spectra of Cr 2p are displayed in Figs. 3 (a1) and (b1) for LSCM and Figs. 4 (a1) and (b1) for LSCMN, respectively. The Cr^{3+} and Cr^{6+} peaks are observed both in the oxidized and reduced samples, but the ratios of Cr^{3+}/Cr^{6+} transform from approximately 80/20 to 84/16 for LSCM and 81/19 to 89/11 for LSCMN after high-temperature reduction, which indicates that part of Cr^{6+} has been chemically reduced into Cr^{3+} in reducing atmosphere.[34] As shown in Figs. 3 (a2), (b2) and Figs. 4 (a2), (b2), the Mn^{4+} is the main chemical state in the oxidized samples, and the Mn^{3+} peaks are observed at 641.2 eV for $2p_{3/2}$ and 653.4 eV for $2p_{1/2}$ in the reduced LSCM as well as 641.5 eV for $2p_{3/2}$ and 653.4 eV for $2p_{1/2}$ in the reduced LSCMN. The concentration of the oxygen vacancy increases with Mn^{4+} transforming to Mn^{3+}, and this will lead to the decrease of the mixed conductivity analyzed later. In order to further confirm the exsolution of nickel nanoparticles, the core level XPS spectra of Ni 2p are shown in Figs. 4 (a3) and (b3). The nickel is in the form of Ni^{2+} in the oxidized LSCMN and the Ni^{2+} $2p_{3/2}$ peak is observed at 854.4 eV overlapped with La^{3+} 3d region as well as the satellite at 864.1 eV shown in Fig. 4 (a3).[35] However, Ni^0 peaks appear in the reduced LSCMN sample observed at 853.3 eV for $2p_{3/2}$ and 869.95 eV for $2p_{1/2}$, respectively, while the Ni^{2+} peaks are observed at the same energy with the oxidized sample as shown in Fig. 4 (b3), which indicates that nickel element partly exists in the form of metal in the reduced sample and further confirms the successful exsolution of nickel nanocatalyst correlated with the XRD and TEM results.

In order to study the electrical properties of LSCM and LSCMN, the dependences of the conductivity on temperature and pO_2 have been examined, respectively. The relative densities of the samples have reached approximately 80%, and the presented conductivities are accordingly normalized.[36-38] Figs. 5 (a) and (b) show the conductivities of LSCM and LSCMN *versus* temperature in air and in 5%H_2/Ar, respectively, which indicate a typical p-type semiconducting behavior of LSCM and LSCMN both in oxidation and reduction state. The conductivities increase with the increased temperature and finally reach approximately 9.86 $S\cdot cm^{-1}$ for LSCM and 15.15 $S\cdot cm^{-1}$ for LSCMN at 800 ºC in air, respectively; however, the maximum conductivities of the reduced samples are approximately 1.04 $S\cdot cm^{-1}$ for LSCM and 1.29 $S\cdot cm^{-1}$ for LSCMN at 800 ºC with pO_2 of approximately 10^{-20} atm, which are close to those measured by other researchers.[25] These conductivity results indicate that the electro-catalytic nickel on ceramic surface or partly in grain boundaries may enhance the electrical conductivity. In addition, the exsolved highly conductive nickel nanoparticles anchoring on the ceramic surface would shorten the diffusion length of free electrons in the ceramics, and make an important contribution in enhancing the conductivity of the reduced LSCMN sample. The extracted grain conduction activation energies in air are given the values of 0.21 eV (80–200 ºC) and 0.27 eV (200–800 ºC) for LSCM and 0.23 eV (80–200 ºC) and 0.28 eV (200–800 ºC) for LSCMN, respectively, and the change in activation energies both for LSCM and LSCMN on heating in air maybe relate to an anticipated rhombohedral to orthorhombic transition.[14] However, lager activation energies are observed under reducing condition with the values of 0.37 eV for LSCM and 0.47 eV for LSCMN, which indicates that the formation of oxygen vacancies under reducing atmosphere leads to the higher ionic conductivity contributed to the total conductivity if the lattice

expansion and the defect clustering effects are not overly inhibiting, even though the electronic conductivity is still dominant.[25,37]

Fig. 6 shows the dependence of the conductivities of LSCM and LSCMN on pO_2. The conductivity of LSCM sample increases from 1.05 to 6.62 $S \cdot cm^{-1}$ with pO_2 ranging from 10^{-18} to 10^{-13} atm and is generally stabilized with pO_2 ranging from 10^{-13} to 10^{-1} atm and finally reaches 9.84 $S \cdot cm^{-1}$ at 800 ºC. The conductivity of LSCMN increases with the same trend from 1.33 to 15.07 $S \cdot cm^{-1}$ with pO_2 increasing from 10^{-18} to 10^{-1} atm. The lessening of the conductivities both for LSCM and LSCMN in the reducing atmosphere is due to the decrease of concentration of charge carriers for p-type conduction which is caused by the formation of oxygen vacancies at low pO_2 atmosphere. In addition, the lattice expansion in reducing atmospheres due to the reduction of transition elements at the B-site may enhance the length of the M-O-M (M = Cr, Mn for LSCM) bond, which would limit the transport of the polaronic and finally result in the decrease of the electronic conductivity at low pO_2.[37] What's more, the stabilization of the conductivity over a wide pO_2 range further indicates the superior redox stability of LSCM and LSCMN ceramics at high temperatures.

Fig. 7 shows the FESEM images and energy-dispersive X-ray spectroscopy (EDS) maps of the surfaces of oxidized and reduced LSCMN patches from the conductivity test bars. As shown in Fig. 7 (a), Cr, Mn and Ni elements have been homogeneously dispersed in the LSCMN sample, which indicates that no phase segregation or element agglomeration exists in the sample after sintering. However, nickel nanoparticles are observed on the surface of the reduced LSCMN, which is confirmed by the Ni element mapping of the EDS pattern and further indicates successful exsolution of the nickel nanocatalyst from LSCM substrate after reduction; while other elements are still homogeneously dispersed shown in Fig. 7 (b). Fig. 8 shows the XRD patterns and SEM images of LSCMN samples in two redox cycles. The XRD results shown in Figs. 8 (a1) and (a2) indicate that the reversible exsolution of nickel is achieved during the LSCMN samples being repeatedly reduced in two redox cycles, nickel nanoparticles are exsolved again under reducing atmosphere from the secondly oxidized LSCMN samples in which nickel nanoparticles dissolve back to form the homogeneous single-phase LSCMN. As shown in Fig. 8 (b1) and (b2), the SEM images of the firstly and secondly reduced LSCMN visually demonstrate the successful reversible exsolution of nickel nanoparticles from LSCM substrate. The mixed conductivities of the porous LSCM and LSCMN electrodes supported on YSZ disks are tested in redox-cycling atmospheres by taking turns flowing air and 5%H_2/Ar shown in Fig. 9. Several conductivity pulses appear after the 5%H_2/Ar flowing over the porous electrode to expose the electrode in a strong reducing atmosphere, and the low pO_2 might lead to the decrease of the concentration of charge carriers which results in the sharp decrease of the mixed conductivity both for LSCM and LSCMN electrodes. The conductivity of the porous LSCM electrode repeatedly shifts between approximately 0.006 and 2 $S \cdot cm^{-1}$, while the conductivity of LSCMN electrode shifts between about 0.006 and 3 $S \cdot cm^{-1}$ in the redox cycling atmospheres at 800 ºC, and that further confirms the superior redox stability of the LSCM or LSCMN electrode material. The improvement of the mixed conductivity of LSCMN electrode in reducing atmosphere is attributed to the presence of nickel metal in the electrode.

Fig. 10 shows the AC impedance spectra of symmetrical cells with the electrodes based on LSCM and LSCMN

measured under different pH_2 at 800 ºC. In this case, all of the series resistances (R_s) have been set as 0 in order to compare the polarization resistances (R_p) which are calculated using Zview software.[39] As shown in Figs. 10 (a1) and (a2), the R_p of the LSCM electrode decreases from approximately 7 to 1.4 $\Omega \cdot cm^2$ with pH_2 increasing from 0 to 80%, which demonstrates that the stronger reducing atmospheres effectively improve the electro-catalytic activity of the composite electrode and therefore enhance the electrode polarizations. Similarly, the R_p of the LSCMN electrode is about 4 $\Omega \cdot cm^2$ in the pure N_2 and finally decreases to approximately 0.7 $\Omega \cdot cm^2$ when pH_2 increases to 80% shown in Figs. 10 (b1) and (b2). Smaller R_p of LSCMN is obtained under each pH_2 compared with LSCM, which is due to that the stronger reducing atmospheres contribute to the exsolution of metallic nickel nanoparticles onto the electrode surface, and that would further enhance the electro-catalytic activity of the composite electrode and improve the electrode performances. Fig. 11 shows the AC impedance spectra of symmetrical cells based on LSCM and LSCMN tested under different pCO at 800 ºC. The R_p decreases with the increased pCO and finally reaches about 13 $\Omega \cdot cm^2$ for the LSCM electrode and 3.5 $\Omega \cdot cm^2$ for the LSCMN electrode when pCO is 4%. Higher pCO leads to stronger reducing atmosphere which similarly benefits to improving electrode performances and the exsolution of metallic nickel nanoparticles and results in the enhancement of the electrode polarizations. The promising polarization of the redox-stable electrode is achieved even in a less reducing atmosphere with small concentration of CO.

Fig. 12 shows the microstructure of the 1-mm-thick YSZ electrolyte-supported solid oxide electrolyzer with LSCMN cathode and LSM anode. Both two porous electrodes adhere very well to the electrolyte with thickness of about 8 μm. The direct CO_2 electrolysis is then investigated in solid oxide electrolyzer with cathode based on LSCM or LSCMN and anode based on LSM under a series of applied voltages ranging from 0 to 2.0 V at 800 ºC. Fig. 13 (a) shows the typical curves of current density *versus* voltage (I-V curves) of the electrolyzers with the applied voltages increasing from 0 to 2.0 V in pure CO_2 at 800 ºC. The open circuit voltages (OCVs) of the electrolyzers reach approximately 0.1 V both for LSCM and LSCMN-based cells, which are consistent well with the CO_2/O_2 concentration cell (0.1–0.6 V) and indicate a good separation between the anodic and cathodic gas. The current density of the electrolyzer based on LSCM is approximately 0.27 $A \cdot cm^{-2}$ with the applied voltage of 2.0 V, and in our previous works direct CO_2 electrolysis with LSCM-based electrolyzer had also been performed by Xu *et al.* and the current density reached 0.18 $A \cdot cm^{-2}$ under 2.0 V at 800 ºC.[21] However, larger current density is achieved in the electrolyzer based on LSCMN for the value of 0.38 $A \cdot cm^{-2}$ under 2.0 V. What's more, the current density of the LSCMN-based electrolyzer increases steeply compared with the LSCM-based electrolyzer. Both of these results demonstrate that the presence of nickel nanocatalyst is beneficial to the improvement of the cathode performances for direct CO_2 electrolysis. Fig. 13 (b) shows the dV/dI curves (total cell resistance) plotted *versus* voltage to study the resistance change of the electrolyzer. At the voltage below 1.0 V, the total cell resistance is mainly constituted of the electrode polarization, which indicates the electrochemical reduction of cathode as the main electrochemical process in electrolyzer at low voltages. However, the ohmic polarization brought along by the ionic transportation in electrolyte becomes the leading

part under the voltage above 1.0 V, which implies that the ionic transport process is the main limitation at high current.

In order to further investigate the anticipated change of cell resistances, *in situ* AC impedance spectra of the electrolyzers based on LSCM and LSCMN cathodes are therefore tested under a series of applied voltages ranging from 1.0 to 2.0 V at 800 ºC shown in Fig. 14. The R_s of the electrolyzers are mainly consistent with the ionic resistance of the YSZ disk and generally stable in the whole range of applied voltages, while the R_p are obviously improved with the voltages increasing from 1.0 to 2.0 V and reach approximately 0.8 $\Omega \cdot cm^2$ for the electrolyzer based on LSCM and 0.65 $\Omega \cdot cm^2$ for the electrolyzer based on LSCMN under 2.0 V, respectively. It is reasonable to assume that the increasing voltage significantly enhances the electrode and improves the cell resistance. It should be noted that there are two semicircles observed on the impedance spectra: the high-frequency arcs (R_1) and low-frequency arcs (R_2). The R_1 is generally stable and an indication of charge transfer, and the improved R_1 of the LSCMN-based electrolyzer indicates the enhanced charge transfer between LSCMN and YSZ. At low frequency, the mass transfer becomes the leading electrode process in the cell, which is due to the dissociative adsorption, gas conversion and species transfer at three-phase boundary. The R_2 is improved with the increased applied voltage, demonstrating the enhanced kinetics of gas conversion at high voltages. What's more, smaller R_2 is achieved in the electrolyzer based on LSCMN, further indicating that the catalytic activity of nickel nanocatalyst improves the electrochemical performances of the composite cathode.

In order to further understand the performances of the CO_2 electrolysis process, short-term performances including current densities and CO production are recorded *versus* time with applied voltages of 1.2, 1.5, 1.8 and 2.0 V at 800 ºC, respectively, as shown in Fig. 15. The current densities increase with the external applied potentials increasing from 1.2 to 2.0 V, which is consistent well with the experimental data shown in Fig. 13 (a); however, at the applied potential of 2.0 V, the current density of the LSCMN-based cell decreases from approximately 0.33 to 0.25 $A \cdot cm^{-2}$ and the same phenomenon is observed under 1.8 V shown in Fig. 15 (b). Under high voltages, the R_p of the cell has been improved and the current density is enhanced, which leads to the high productions of CO as well as high demand of CO_2 at the three phase boundary between the electrolyte, the cathode and the gas. However, the transfer of CO_2 through the cathode may be limited by the structure and the catalytic activity of cathode, which may cause the decrease of current densities, while the current efficiencies also stay unaltered shown in Fig. 16. By comparison, the current densities under lower voltages remain stable and the long-term performances under 1.4 V have been investigated later. The productions of CO of the electrolyzers based on LSCM and LSCMN increase under the same tendency as the current density and reaches the maximum of 1.06 $ml \cdot min^{-1} \cdot cm^{-2}$ for the LSCM-based electrolyzer as well as 1.9 $ml \cdot min^{-1} \cdot cm^{-2}$ for the LSCMN-based electrolyzer under 2.0 V, respectively. It is obvious that the catalytic activity of the nickel nanocatalyst is able to effectively improve the cathode performance and significantly increase the production of CO with the accompanied increased electrocatalytic activity. Fig. 16 shows the current efficiencies of the CO_2 electrolysis with the solid oxide electrolyzers based on LSCM and LSCMN. The current efficiency of CO_2 electrolysis is approximately 55% for the LSCM-based cell which is consistent with 58% in our previous

work by Xu *et al.* for LSCM-based electrolyzer.[21] In comparison, it is significantly enhanced to almost 85% for the LSCMN-based cell because of the synergetic effect of the nickel nanocatalyst and redox-stable LSCM substrate that improves the cathode performances for CO_2 electrolysis. In order to investigate the long-term stability of the LSCMN composite cathode, direct CO_2 electrolysis is performed with the LSCMN-based electrolyzer under a fixed voltage of 1.4 V for 21 h at 800 ºC, and the flow rate of CO_2 stays the same with the short-term CO_2 electrolysis. As shown in Fig. 17, the current efficiencies and productions of CO almost remain stable during a longer time under the same condition, which confirms the excellent long-term stability of the LSCMN composite cathode for direct CO_2 electrolysis.

Conclusions

In this work, the *in situ* grown nickel nanocatalyst is anchored on surface of the redox-stable chromate cathode to improve the catalytic activity for direct CO_2 electrolysis in an oxide-ion-conducting solid oxide electrolyzer. And the exsolution or dissolution of the nickel nanoparticles is demonstrated to be completely reversible in redox cycles. Anticipatively significant improvements are obtained in electrochemical performances and current efficiency of the electrolyzer based on nickel-anchored LSCM for the direct CO_2 electrolysis at 800 ºC. The current efficiency is enhanced to approximately 85% attributed to the presence of nickel nanocatalyst in the cathode. What's more, the synergetic effect of the catalytic-active nickel with the redox-stable LSCM results in a remarkably stability of the composite cathode for direct CO_2 electrolysis in the short term.

Acknowledgement

This work is supported by the Natural Science Foundation of China No. 21303037, China Postdoctoral Science Foundation No. 2013M53150 and the Fundamental Research Funds for the Central Universities No. 2012HGZY0001.

Notes and references

[a] Department of Energy Materials, School of Materials Science and Engineering, Hefei University of Technology, No.193 Tunxi Road, Hefei, Anhui 230009, China.

[b] Key Laboratory of Advanced Functional Materials and Devices, Hefei University of Technology, No.193 Tunxi Road, Hefei, Anhui 230009, China.

*Corresponding: xiekui@hfut.edu.cn; +86-551-62901012

1 C. R. Jiang, J. J. Ma, A. D. Bonaccorso and J. T. S. Irvine, *Energy Environ. Sci.*, 2012, **5**, 6973-6980.

2 S. J. Wang, A. Inoishi, J. Hong, Y. Ju, H. Hagiwara, S. Ida and T. Ishihara, *J. Mater. Chem.*, 2013, **1**, 12455-12461.

3 N. S. Spinner, J. A. Vega and W. E. Mustain, *Catal. Sci. Technol.*, 2012, **2**, 19-28.

4 M. Chen, J. V. T. Hogh, J. U. Nielsen, J. J. Bentzen, S. D. Ebbesen and P. V. Hendriksen, *Fuel Cells*, 2013, **13**, 628-645.

5 E. Ivers-Tiffée, A. Weber and D. Herbstritt, *J. Eur. Ceram. Soc.*, 2001, **21**, 1805-1811.

6 X. L. Yue and J. T. S. Irvine, *Electrochem. Solid State Lett.*, 2012, **15**, B31-B34.

7 S. S. Li, Y. X. Li, Y. Gan, K. Xie and G. Y. Meng, *J. Power Sources*, 2012, **218**, 244-249.

8 A. Hauch, S. D. Ebbesen, S. H. Jensen and M. Mogensen, *J. Mater. Chem.*, 2008, **18**, 2331-2340.

9 X. D. Yang and J. T. S. Irvine, *J. Mater. Chem.*, 2008, **18**, 2349-2354.

10 P. Kim-Lohsoontorn and J. Bae, *J. Power Sources*, 2010, **196**, 7161-7168.

11 S. D. Ebbesen and M. Mogensen, *J. Power Sources*, 2009, **193**, 349-358.

12 Z. L. Zhan, W. Kobsiriphat, J. R. Wilson, M. Pillai, I. Kim and S. A. Barnett, *Energy Fuels*, 2009, **23**, 3089-3096.

13 S. W. Tao and J. T. S. Irvine, *Chem. Mater.*, 2004, **16**, 4116-4121.

14 S.W. Tao and J. T. S. Irvine, *Nat. Mater.*, 2003, **2**, 320-323.

15 G. Kim, G. Corre, J. T. S. Irvine, J. M. Vohs and R. J. Gorte, *Electrochem. Solid State Lett.*, 2008, **11**, B16-B19.

16 R. M. Xing, Y. R. Wang, S. H. Liu and C. Jin, *J. Power Sources*, 2012, **208**, 276-281.

17 S. W. Zha, P. Tsang, Z. Cheng and M. L. Liu, *J. Solid. State. Chem.*, 2005, **178**, 1844-1850.

18 J. C. Ruiz-Morales, J. Canales-Vázquez, B. Ballesteros-Pérez, J. Pena-Martínez, D. Marrero-López, J.T.S. Irvine and P. Nunaz, *J. Eur. Ceram. Soc.*, 2007, **27**, 4223-4227.

19 G. J. Wu, K. Xie, Y. C. Wu, W. T. Yao and J. E. Zhou, *J. Power Sources*, 2013, **232**, 187-192.

20 X. L. Yue and J. T. S. Irvine, *Solid State Ionics*, 2012, **225**, 131-135.

21 S. S. Xu, S. S. Li, W. T. Yao, D. H. Dong and K. Xie, *J. Power Sources*, 2013, **230**, 115-121.

22 Z. Cheng, J. H. Wang, Y. M. Choi, L. Yang, M. C. Lin and M. L. Liu, *Energy Environ. Sci.*, 2011, **4**, 4380–4409.

23 L. D. Fan, C. Y. Wang and B. Zhu, *Nano Energy*, 2012, **1**, 631-639.

24 T. Truong, C. K. Nguyen, T. V. Tran, T. T. Nguyen and N. T. S. Phan, *Catal. Sci. Technol.*, 2014, **4**, 1276-1285.

25 T. Jardiel, M. T. Caldes, F. Moser, J. Hamon, G. Gauthier and O. Joubert, *Solid State Ionics*, 2010, **181**, 894-901.

26 D. Neagu, G. Tsekouras, D. N. Miller, H. Ménard and J. T. S. Irvine, *Nat. Chem.*, 2013, **5**, 916-923.

27 D. M. Bastidas, S. W. Tao and J. T. S. Irvine, *J. Mater. Chem.*, 2006, **16**, 1603-1605.

28 L Shi, C. Y. Zeng, Y. Z. Jin, T. J. Wang and N. Tsubaki, *Catal. Sci. Technol.*, 2012, **2**, 2569-2577.

29 F. L. Chen and M. L. Liu, *J. Eur. Ceram. Soc.*, 2001,**21**, 127-134.

30 G. B. Jung and T. J. Huang, *J. Mater. Sci.*, 2013, **38**, 2461-2468.

31 S. W. Tao and J. T. S. Irvine, *Solid State Ionics*, 2008, **179**, 725-731.

32 K. Xie, R. Q. Yan and X. Q. Liu, *Electrochem. Commun.*, 2009, **11**, 1618-1622.

33 S. Estemirova, A. Fetisov, V. Balakirev and S. Titova, *J. Supercond. Nov. Magn.*, 2007, **20**, 113-116.

34 Y. X. Li, Y. Wang, W. Doherty, K. Xie and Y. C. Wu, *ACS Appl. Mater. Inter.*, 2013, **5**, 8553-8562.

35 A. T. Fulmer, J. Dondlinger and M. A. Langell. *Appl. Surf. Sci.*, 2014, **305**, 544-553.

36 D. Neagu and J. T. S. Irvine, *Chem. Mater.*, 2010, **22**, 5042-5053.

37 S. W. Tao and J. T. S. Irvine, *J. Electrochem. Soc.*, 2004, **151**, A252-A259.

38 V. V. Kharton, A. V. Kovalevsky, A. P. Viskup, F. M. Figueiredo, A. A. Yaremchenko, E. N. Naumovich and F. M. B. Marques, *J. Eur. Ceram. Soc.*, 2001, **21**, 1763-1767.

39 A. Rolle, V. Thoreton, P. Rozier, E. Capoen, O. Mentre, B. Boukamp and S. Daviero-Minaud, *Fuel Cells*, 2012, **12**, 288-301.

Captions

Fig. 1 XRD Rietveld refinement patterns of the (a1) oxidized LSCM; (a2) reduced LSCM; (b1) oxidized LSCMN and (b2) reduced LSCMN, respectively.

Fig. 2 HRTEM images of the (a1) oxidized LSCM; (a2) reduced LSCM; (b1) oxidized LSCMN and (b2) reduced LSCMN, respectively.

Fig. 3 Cr 2p and Mn 2p X-ray photoelectron spectroscopies of (a) oxidized and (b) reduced LSCM, respectively.

Fig. 4 Mn 2p, Cr 2p and Ni 2p X-ray photoelectron spectroscopies of (a) oxidized and (b) reduced LSCMN, respectively.

Fig. 5 The conductivities of LSCM and LSCMN *versus* temperature in (a) air and (b) 5%H_2/Ar until 800 ºC, respectively.

Fig. 6 The conductivities of LSTO and LSTCO *versus* pO_2 at ranging from 10^{-1} to 10^{-18} atm at 800 °C, respectively.

Fig. 7 FESEM images and EDS maps of (a) oxidized and (b) reduced LSCMN, respectively.

Fig. 8 XRD and SEM results of LSCMN samples in redox cycles: (a) XRD patterns of repeatedly reduced LSCMN and (b) SEM images of the repeatedly reduced LSCMN, respectively.

Fig. 9 Mixed conductivities of (a) the LSCM electrode and (b) the LSCMN electrode in redox-cycling atmospheres at 800 °C, respectively.

Fig. 10 The AC impedance spectra of symmetrical cells (a) LSCM/YSZ/LSCM and (b) LSCMN/YSZ/LSCMN at different pH_2 at 800 ºC, respectively.

Fig. 11 The AC impedance spectra of symmetrical cells (a) LSCM/YSZ/LSCM and (b) LSCMN/YSZ/LSCMN at different *p*CO at 800 ºC, respectively.

Fig. 12 Cross sectional SEM micrograph for the solid oxide electrolyzer of Ag/LSCMN-SDC/YSZ/LSM-SDC/Ag.

Fig. 13 (a) Current-voltage curves of the solid oxide electrolyzers with cathodes based on LSCM and LSCMN fed with pure CO_2 at 800 ºC; (b) the *d*V/*d*I (cell resistance) of solid oxide electrolyzers based on LSCM and LSCMN composite cathodes.

Fig. 14 The AC impedance spectra of solid oxide electrolyzers with cathodes based on (a) LSCM and (b) LSCMN fed with pure CO_2 at 800 ºC, respectively.

Fig. 15 Performances and productions of CO in the solid oxide electrolyzers (a) LSCM-SDC/YSZ/LSM-SDC and (b) LSCMN-SDC/YSZ/LSM-SDC under different applied voltages at 800 ºC, respectively.

Fig. 16 Current efficiencies of direct CO_2 electrolysis in the solid oxide electrolyzers LSCM-SDC/YSZ/LSM-SDC and LSCMN-SDC/YSZ/LSM-SDC under different applied voltages at 800 ºC, respectively.

Fig. 17 Current efficiencies and productions of CO of long-term CO_2 electrolysis with electrolyzer LSCMN-SDC/YSZ/LSM-SDC under 1.4 V at 800 ºC.

Fig. 1

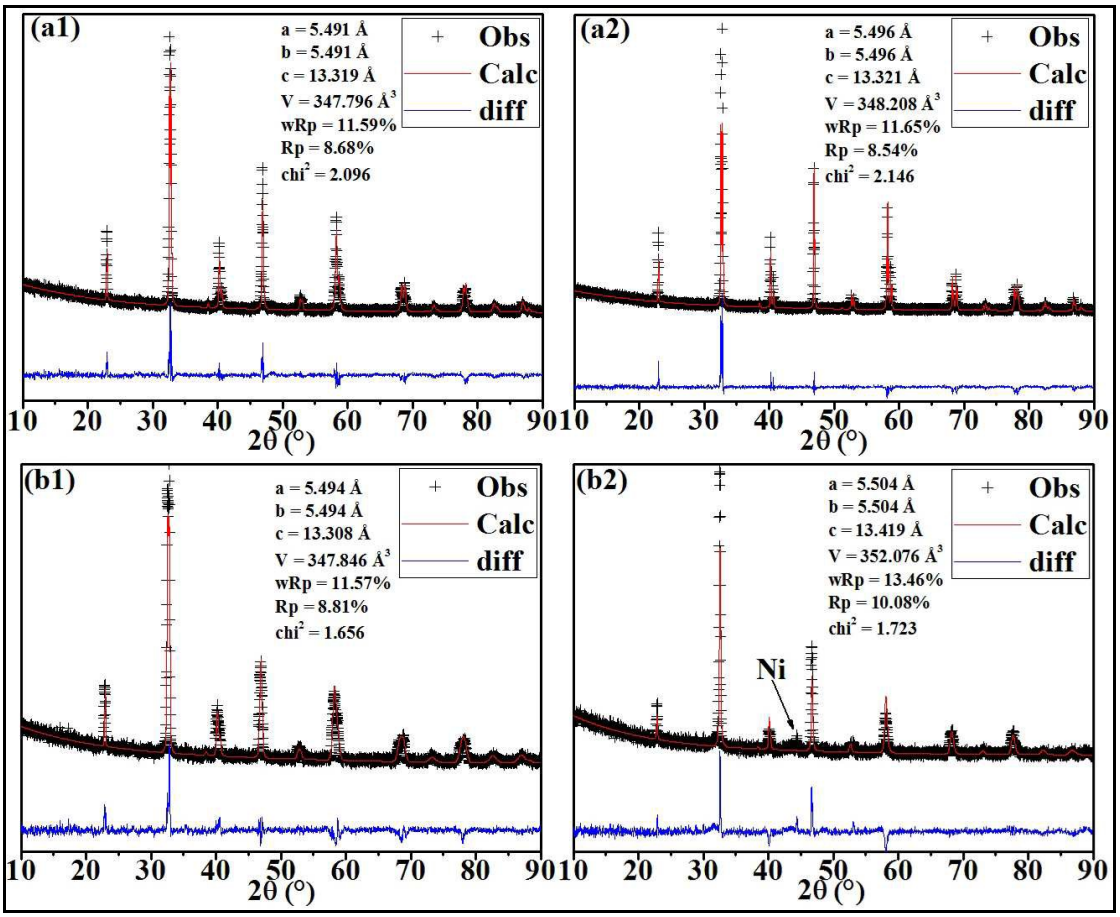

Fig. 2

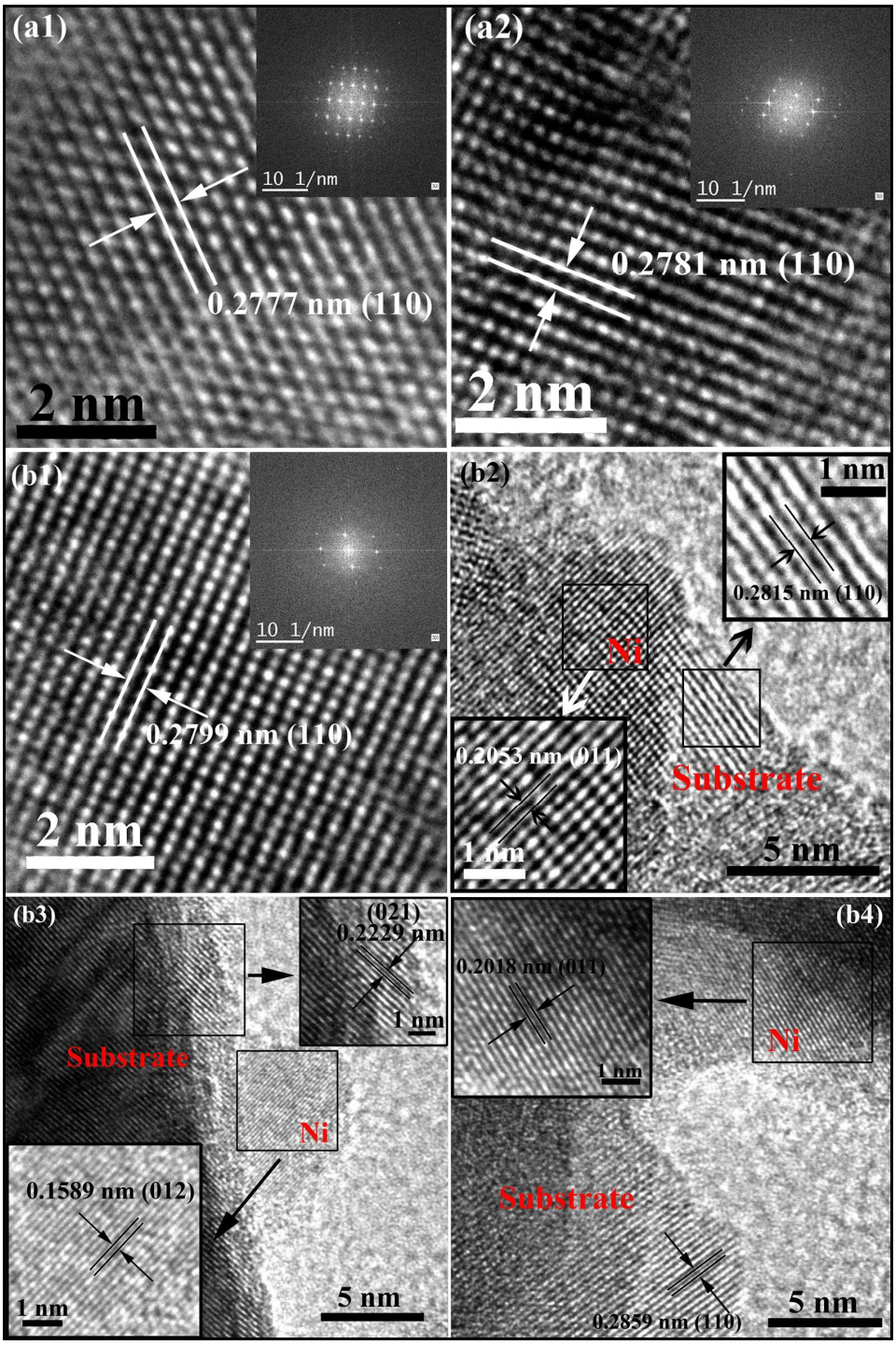

Fig. 3

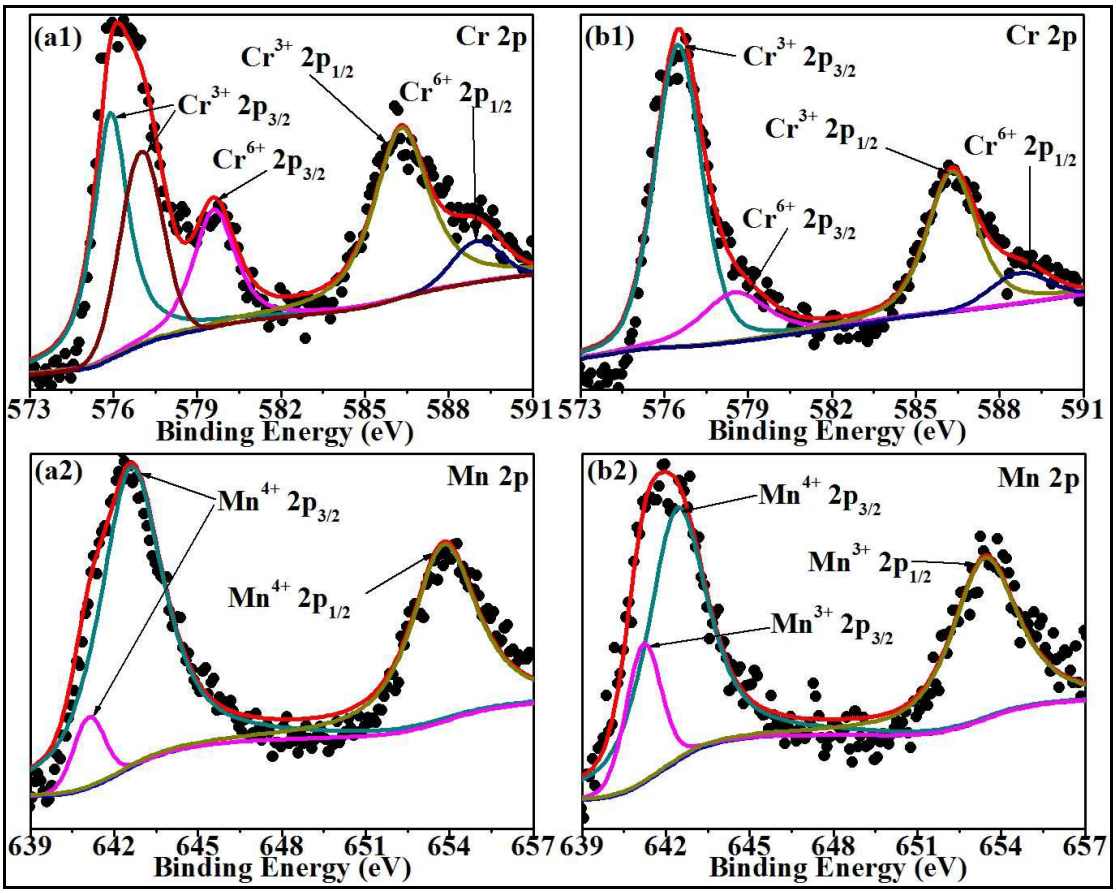

Fig. 4

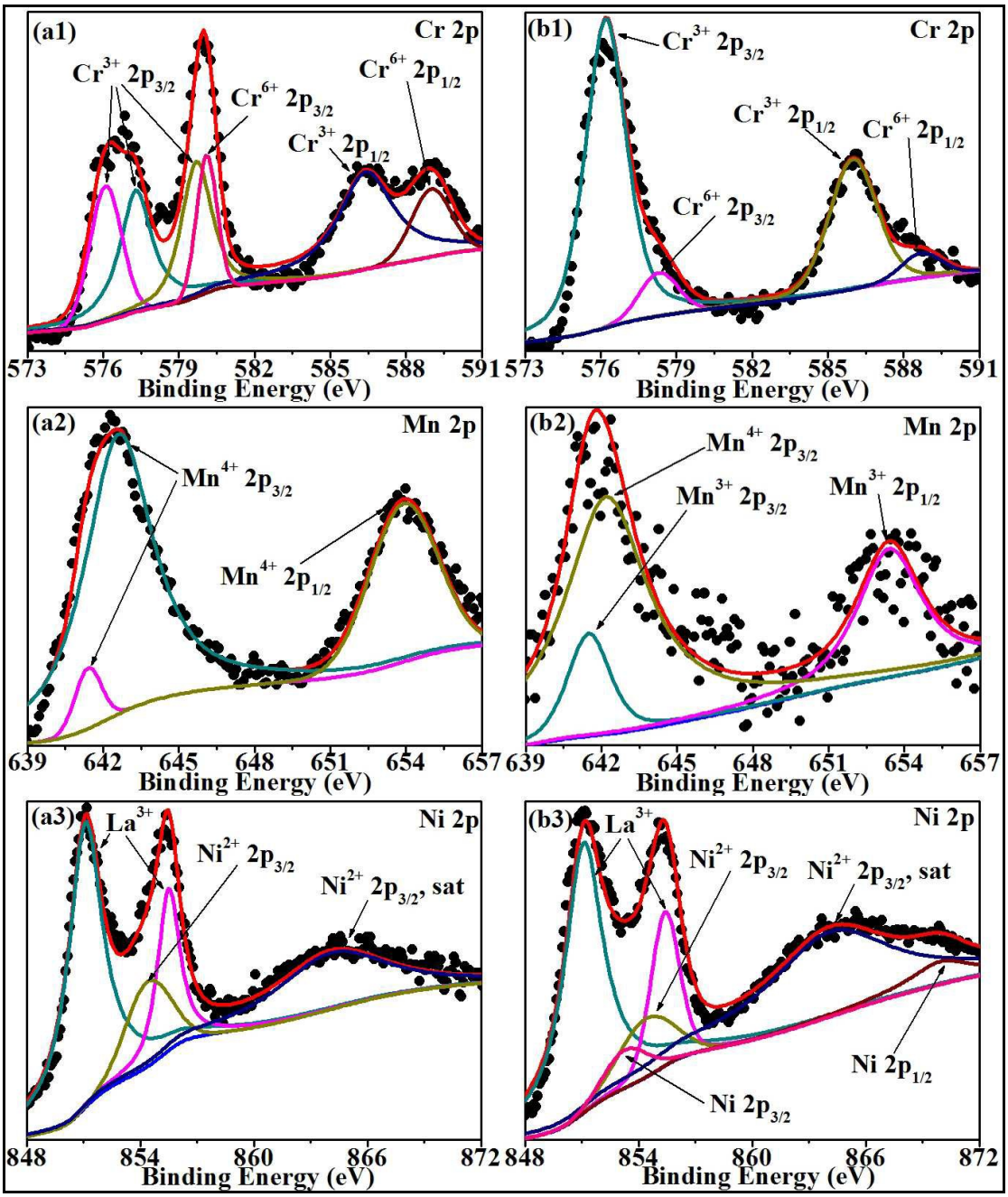

Fig. 5

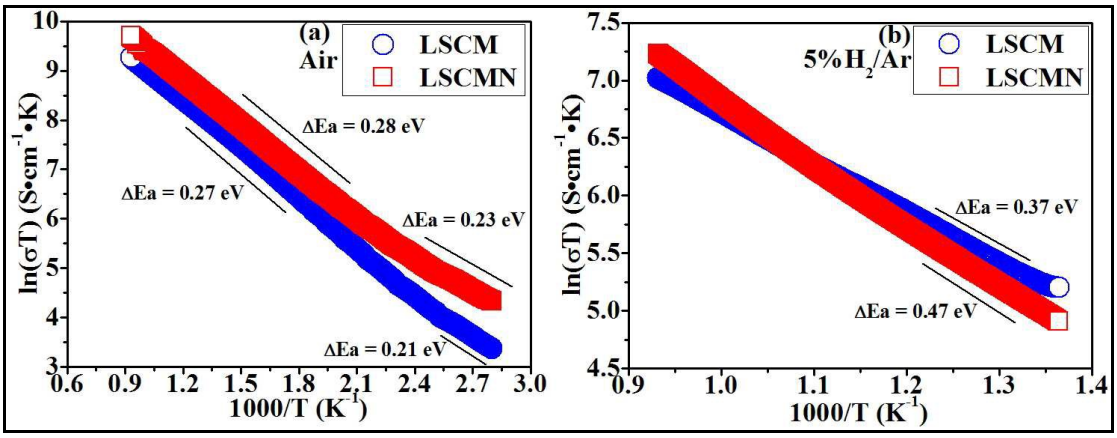

Fig. 6

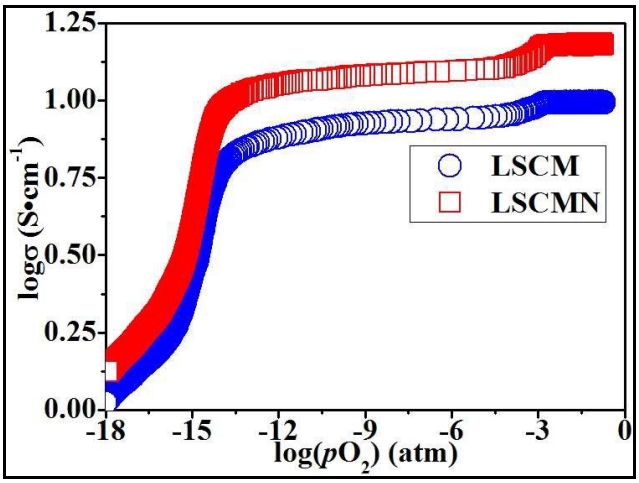

Fig. 7

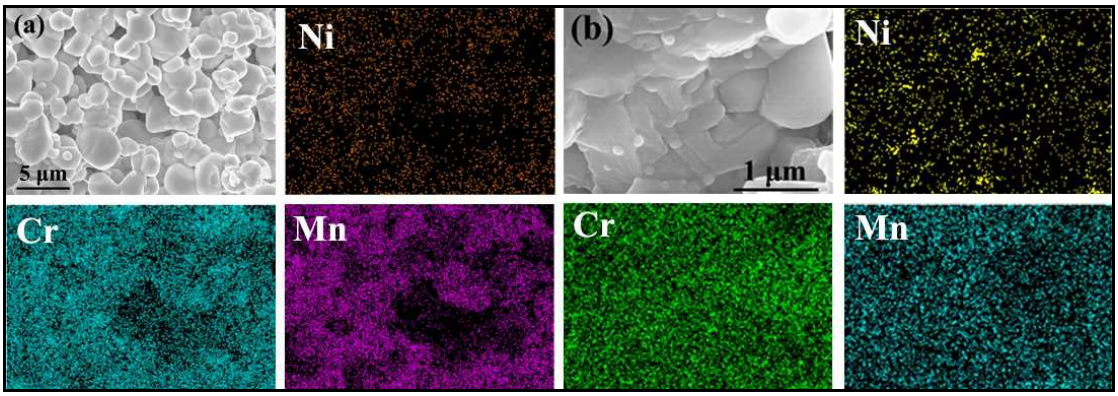

Fig. 8

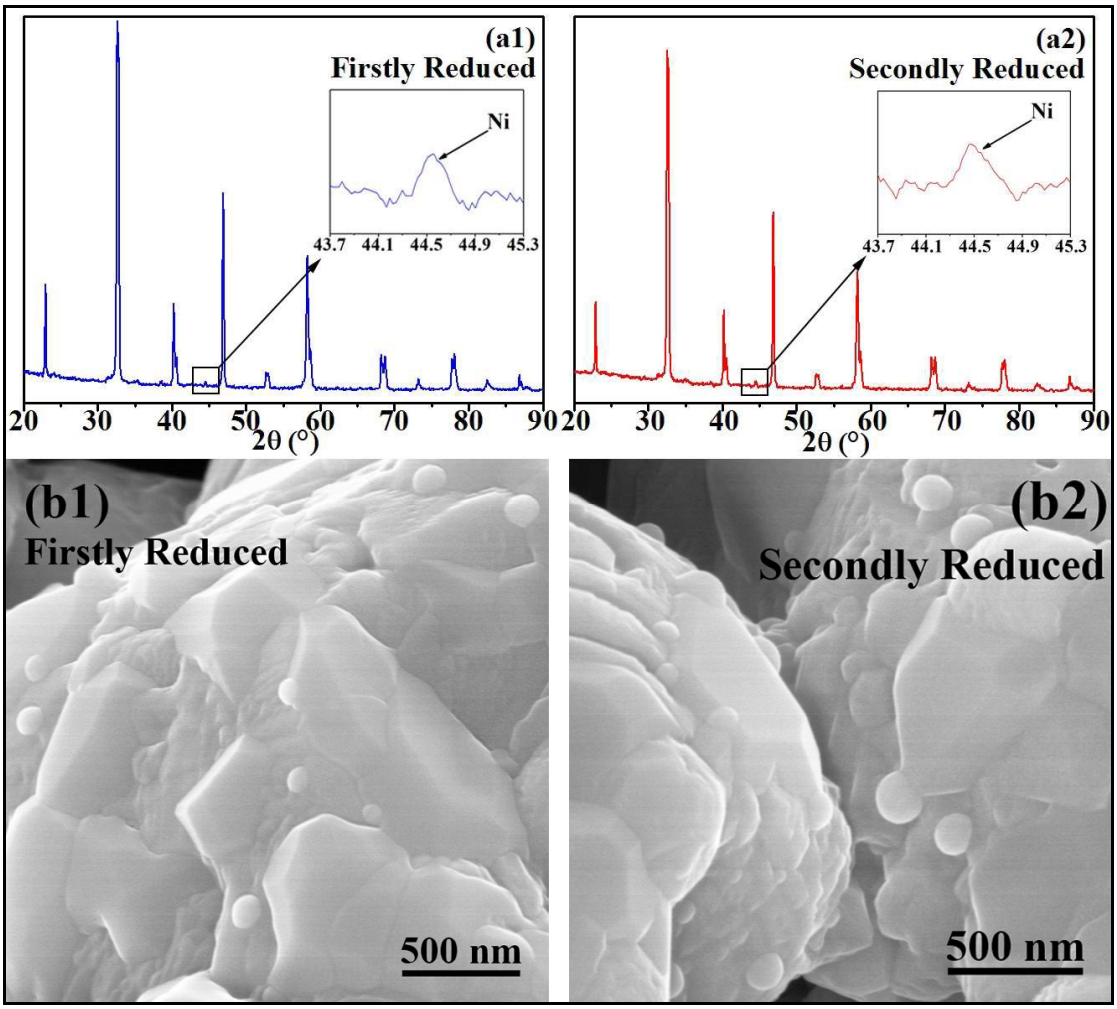

Fig. 9

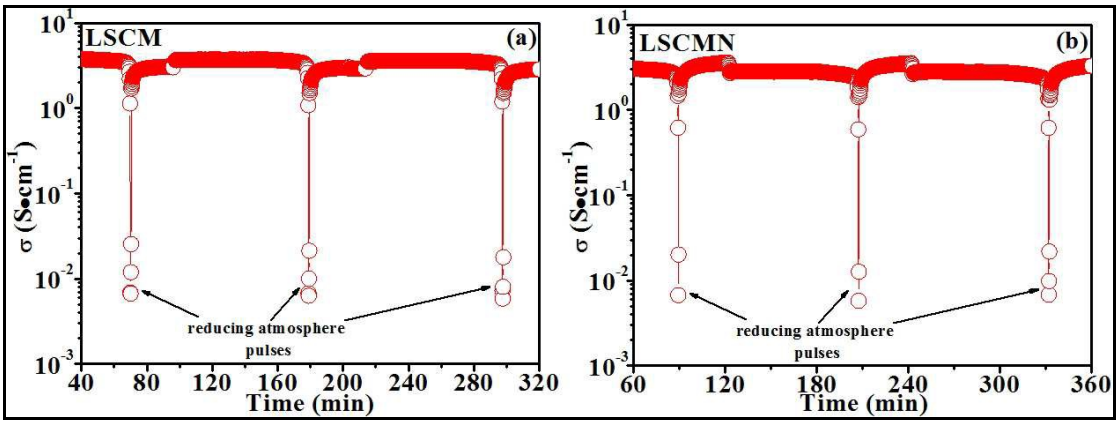

Fig. 10

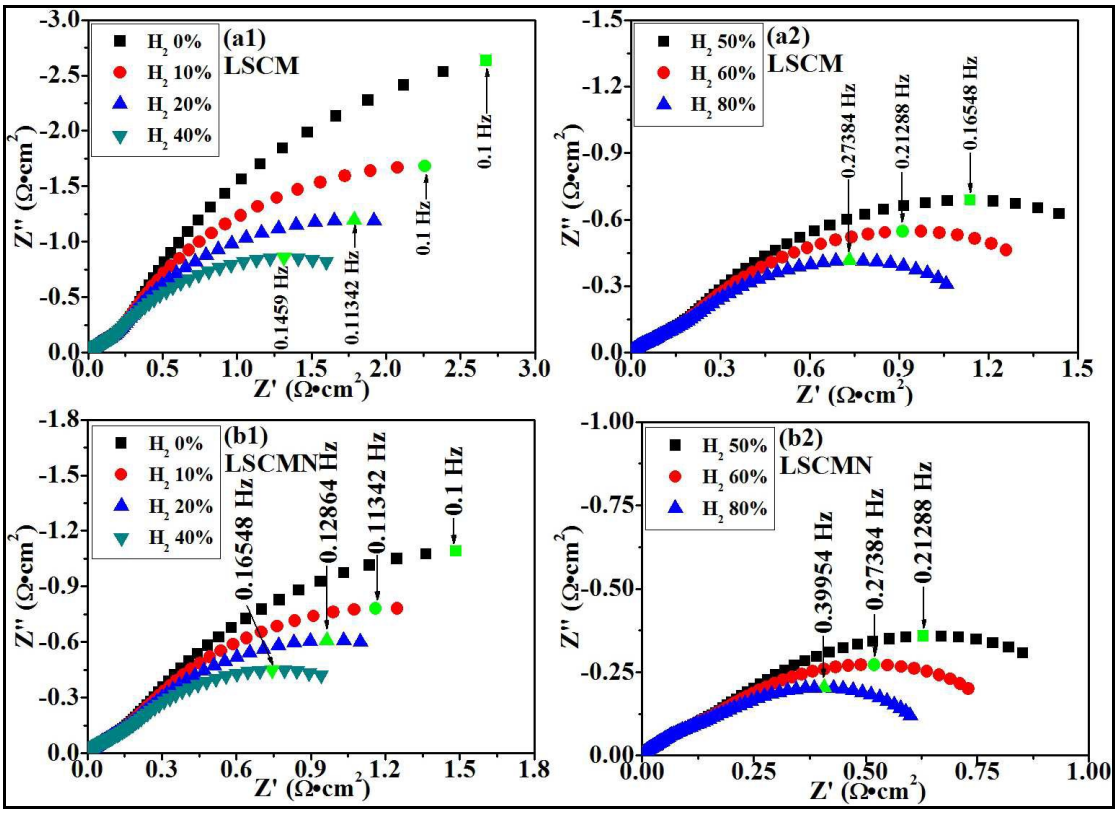

Fig. 11

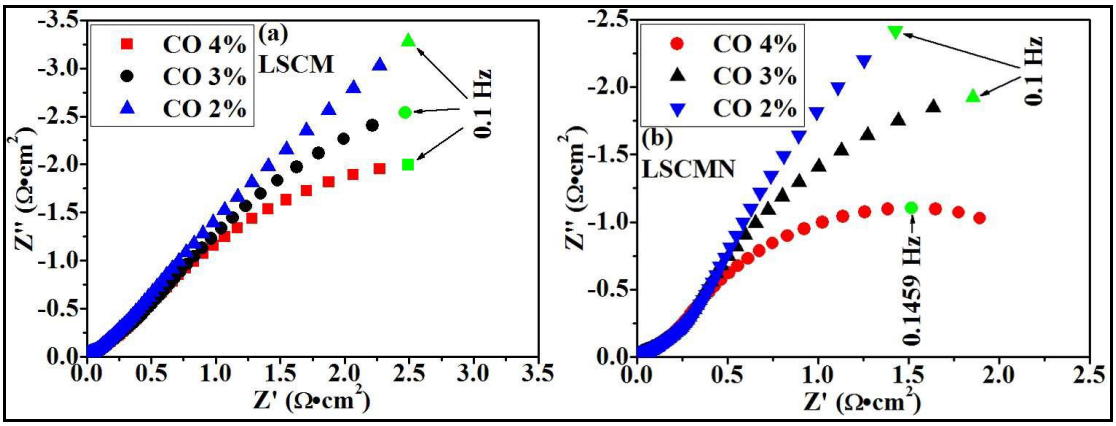

Fig. 12

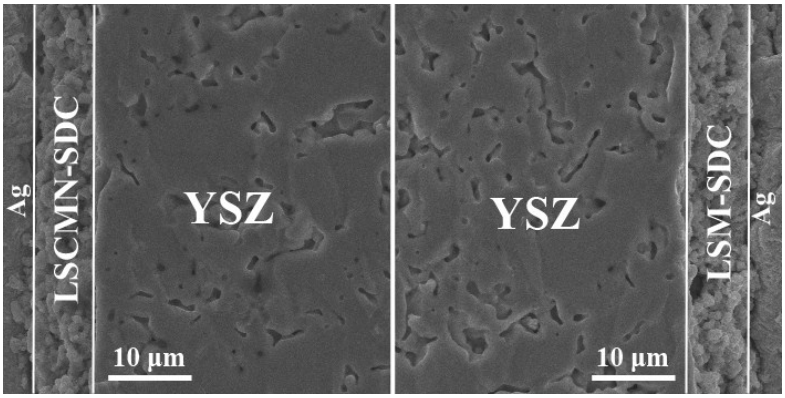

Fig. 13

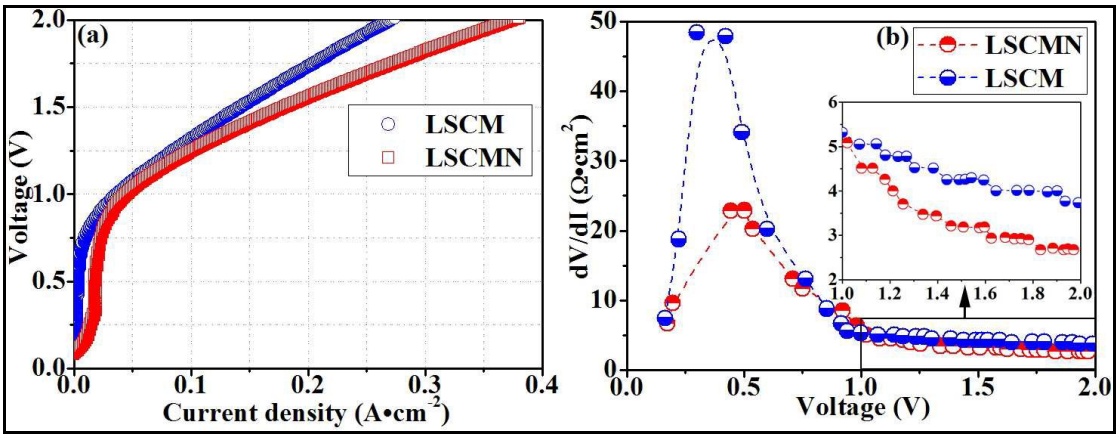

Fig. 14

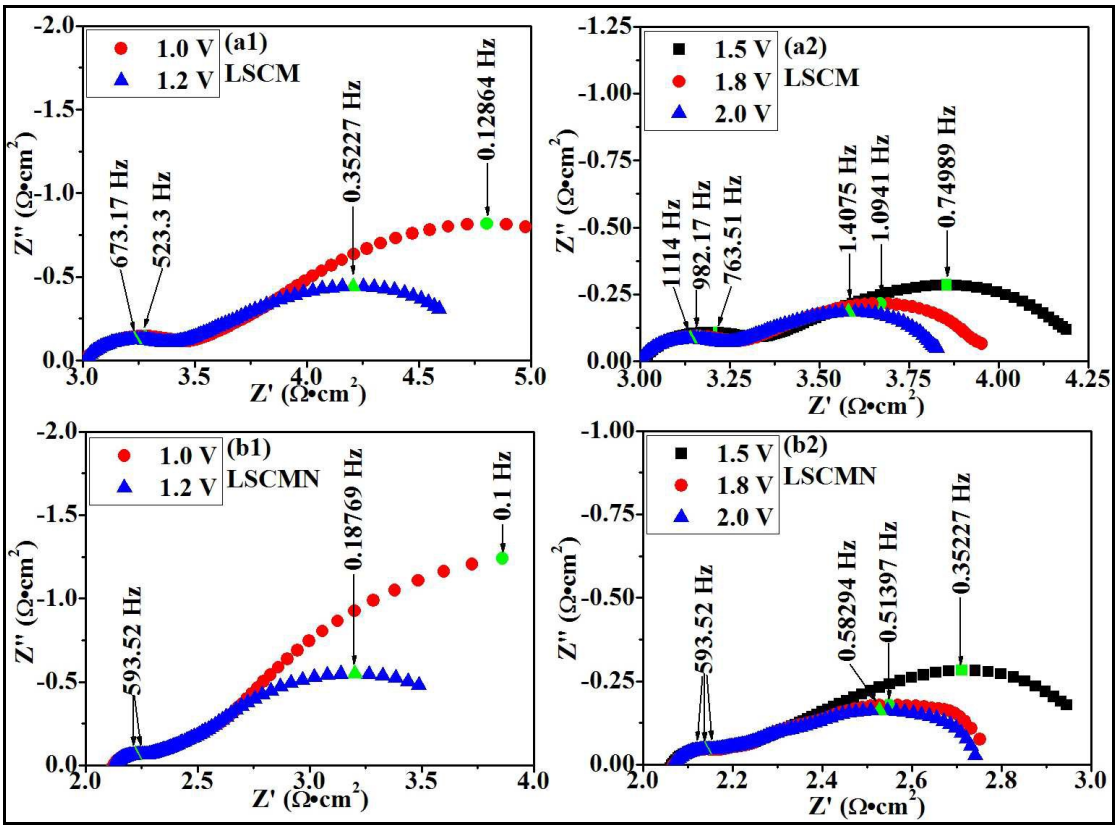

Fig. 15

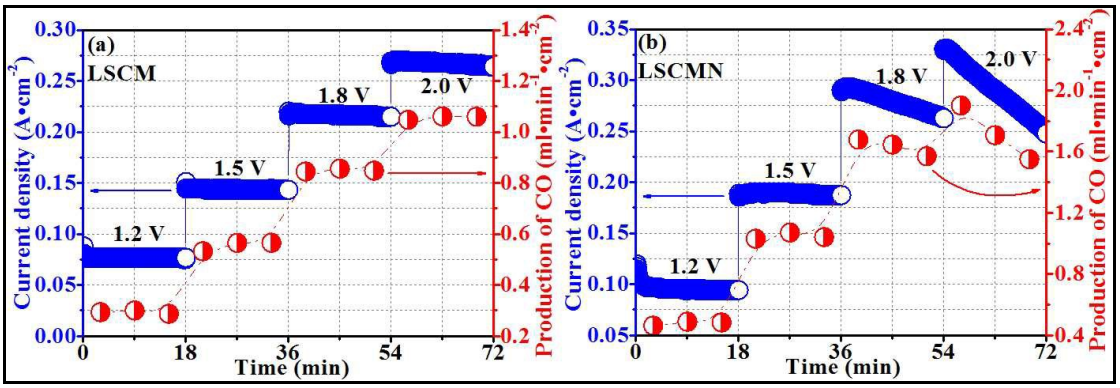

Fig. 16

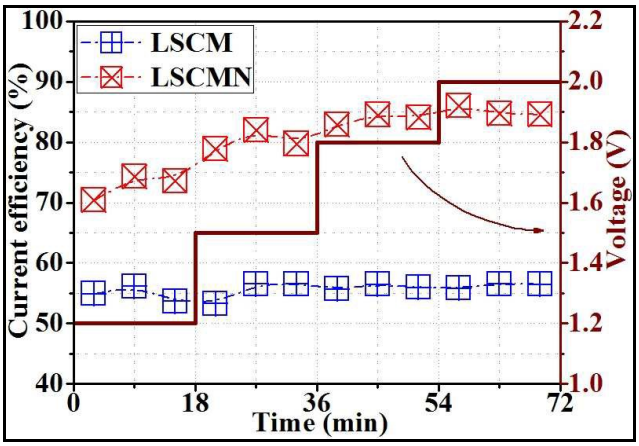

Fig. 17